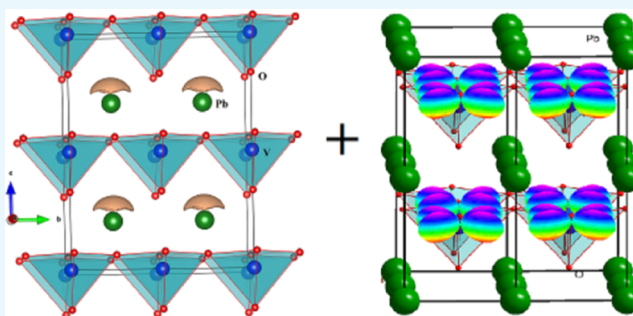


Giant Magnetolectric Coupling in Multiferroic $\text{PbTi}_{1-x}\text{V}_x\text{O}_3$ from Density Functional CalculationsLokanath Patra,^{†,‡,§} Ravindran Vidya,[§] Helmer Fjellvåg,^{||} and Ponniah Ravindran^{*,†,‡,§}[†]Department of Physics and [‡]Simulation Center for Atomic and Nanoscale MATerials, Central University of Tamil Nadu, Thiruvavur 610005, Tamil Nadu, India[§]Department of Medical Physics, Anna University, Chennai 600025, India^{||}Center for Materials Science and Nanotechnology and Department of Chemistry, University of Oslo, P.O. Box 1033, Blindern, N-0315 Oslo, Norway

Supporting Information

ABSTRACT: Giant magnetolectric coupling is a very rare phenomenon that has gained much attention in the past few decades due to fundamental interest as well as practical applications. Here, we have successfully achieved giant magnetolectric coupling in $\text{PbTi}_{1-x}\text{V}_x\text{O}_3$ ($x = 0-1$) using a series of generalized gradient-corrected GGA (generalized gradient approximation), including on-site Coulomb repulsion (U)-corrected spin-polarized calculations based on accurate density functional theory. Our total energy calculations show that $\text{PbTi}_{1-x}\text{V}_x\text{O}_3$ stabilizes in C-type antiferromagnetic ground state for $x > 0.123$. With the substitution of V into PbTiO_3 , the tetragonal distortion is highly enhanced accompanied by a linear increase in polarization. In addition, our band structure analysis shows that for lower x values, the tendency to form two-dimensional magnetism of $\text{PbTi}_{1-x}\text{V}_x\text{O}_3$ decreases. The orbital magnetic polarization was calculated with self-consistent field method by including orbital polarization correction in the calculation as well as from the computed X-ray magnetic dichroism spectra. A nonmagnetic metallic ground state is observed for the paraelectric phase for V concentration (x) = 1 competing with a volume change of 10% showing a large magnetovolume effect. Our orbital-projected density of states as well as orbital ordering analysis suggest that the orbital ordering plays a major role in the magnetic-to-nonmagnetic transition when going from ferroelectric to paraelectric phase. The calculated magnetic anisotropic energy shows that the direction [110] is the easy axis of magnetization for $x = 1$ composition. The partial polarization analysis shows that the Ti/V–O hybridization majorly contributes to the total electrical polarization. The present study adds a new series of compounds to the magnetolectric family with rarely existing giant coupling between electric- and magnetic-order parameters. These results show that such kind of materials can be used for novel practical applications where one can change the magnetic properties drastically (magnetic to nonmagnetic, as shown here) with external electric field and vice versa.



INTRODUCTION

The promising coupling between electric- and magnetic-order parameters and the potential to manipulate one by the application of the other have attracted much attention in the past few decades. Interest in the research on materials with such coupling has grown because of their wide range of application in multifunctional devices.^{1–5} The ultimate goal of this research is to obtain single-phase multiferroics with strong coupling between ferroelectric- and magnetic-order parameters at room temperature. There has been a considerable recent interest in developing lone pair-based magnetolectrics because of their high value of electrical polarization. Examples of such composites include $\text{BiFeO}_3\text{–LaFeO}_3$,⁶ $\text{BiFeO}_3\text{–SrTiO}_3$,⁷⁷ $\text{BiFeO}_3\text{PbTiO}_3$,⁸⁸ $\text{BiFeO}_3\text{–BiCoO}_3$,⁹ $\text{LaFeO}_3\text{–PbTiO}_3$,¹⁰¹⁰ $\text{BiFeO}_3\text{–BaTiO}_3$,¹¹¹¹ $\text{BiCoO}_3\text{–BaTiO}_3$,¹² etc. PbTiO_3 (PTO) is a perovskite ferroelectric material with a Curie temperature of 490 °C and a large tetragonal distortion

with $c/a = 1.06^{13}$ at room temperature. But it is nonmagnetic (NM) due to the absence of d electrons. The Ti atom can be substituted with some magnetic ions, as a result of which the new compound can be expected to produce both magnetic and ferroelectric behaviors. PTO-based magnetolectrics could be much more interesting because of the existence of two types of mechanisms for ferroelectricity, i.e., lone pair electrons from Pb^{2+} and d⁰-ness from Ti^{4+} . So, here we examine the magnetolectric properties of a PTO-based multiferroic series, i.e., $\text{PbTi}_{1-x}\text{V}_x\text{O}_3$ ($x = 0, 0.25, 0.33, 0.50, 0.67, 0.75, 1$), where the 6s electrons of Pb^{2+} and the d⁰-ness of Ti^{4+} stabilize the ferroelectricity and the V induces magnetism.

Received: April 24, 2019

Accepted: July 12, 2019

Published: September 30, 2019

On the other hand, PbVO_3 (PVO), which is a member of this series ($x = 1$), has gained much interest in the last few years as a strong candidate for multiferroic oxide due to its large electric polarization. Although it is isostructural with PTO, it shows large tetragonal distortion ($c/a = 1.229$). Isolated layers of corner-shared VO_3 pyramids form a layer-type perovskite structure with a space group $P4mm$.¹⁴ PVO has been proposed to have an antiferromagnetic ordering and a ferroelectric polarization as large as $152 \mu\text{C}/\text{cm}^2$ due to the presence of large structural distortions.^{14–18} To this point, however, the true magnetic structure and the multifunctional nature of this material are controversial to researchers. Shpanchenko et al.¹⁴ found no long-range magnetic ordering with their neutron powder diffraction measurements down to 1.5 K. Belik et al.¹⁶ proposed that PVO is a two-dimensional (2D) spin-half square-lattice strongly frustrated antiferromagnet due to the antiferromagnetic interactions of the next nearest neighbors. Using magnetic susceptibility and specific heat measurements as well as band structure calculations, Tsirlin¹⁹ confirmed that the $S = 1/2$ square lattice of vanadium $4+$ ions in PVO is strongly frustrated due to the next-nearest-neighbor antiferromagnetic interactions and no long-range magnetic ordering was found down to 1.8 K. Due to the presence of defects or ferromagnetic (FM) impurities in the sample, it has been very difficult to clarify the intrinsic magnetic property in PVO. Oka et al.²⁰ investigated the magnetic properties of PVO by preparing a multidomain single crystal without any magnetic impurity. The broad maximum centered around 180 K in the temperature-dependent magnetization curve indicates the presence of two-dimensional antiferromagnetism. Muon spin rotation measurement displayed the presence of a long-range order below 43 K. The epitaxial thin films of PVO have been grown²¹ using pulsed laser deposition, which brings a step forward to synthesis of multiferroic materials outside of high-temperature and high-pressure techniques to realize devices with multifunctionalities. In another study on PVO thin films by Kumar et al.,²² a transition from a ferroelectric-only state to a ferroelectric and magnetic state was observed below 100–130 K using second-harmonic generation and X-ray linear dichroism. Experimental electron energy loss spectroscopy investigation on V–L edge shows that V in the PVO thin films is in the V^{4+} state, resulting in a d^1 state.²³

PVO was also investigated computationally by different researchers. First-principles calculations were made by Uratani et al.¹⁷ for PVO along with BiCoO_3 . They found that the easy axes of spin are different: $[110]$ in PVO and $[001]$ in BiCoO_3 even though both have similar crystal structure. A spin spiral structure was predicted by Solovyev²⁴ to analyze the absence of long-range magnetic ordering in PVO. Calculations along with experiments were performed by Parveen et al.²⁵ in 2012 to study the thermal properties of PVO, and the results confirmed the observations made by Tsirlin et al.¹⁹ Ming et al.²⁶ made a comparative study of the structural, electronic, magnetic, and phase-transition properties in which various exchange-correlation (XC) functionals were used and found that PVO is a 2D C-type antiferromagnetic (C-AF), where the d^1 electron of the V^{4+} ion occupies the d_{xy} orbital. A ferroelectric-to-paraelectric phase transition at 1.75 GPa was also noted. Zhou et al.²⁷ revisited the structural transitions in PVO using a series of X-ray diffraction measurements and first-principles calculations. They found that the C-AF insulating and NM metallic states are the ground states for tetragonal and

cubic phases, respectively. They have also noted a non-centrosymmetric tetragonal-to-centrosymmetric cubic perovskite structural phase transition in the pressure range of 2.7–6.4 GPa.

Milošević et al.²⁸ performed ab initio calculations to study the electronic structure and optical properties of PVO (and BiCoO_3). Using first-principles density functional theory (DFT) calculations, Ming et al.²⁹ showed a first-order tetragonal-to-cubic phase transition with a volume collapse of 11.6% under a uniaxial pressure of 1.2 GPa accompanied by a C-AF insulator to an NM metal. Kadiri et al.³⁰ studied the magnetic properties of PVO using first-principles calculations and Monte Carlo simulations and determined PVO as an $S = 1/2$ antiferromagnet with a Néel temperature (T_N) of 182 K. Recently, Oka et al.³¹ have examined the cubic phase of PVO under high pressure on experimental and theoretical bases. They determined the transition pressure to be 3 GPa and showed that above this pressure, the semiconductor-to-metal transition associated with the structural transition (tetragonal to cubic) occurs.

There are some reports about the transition-metal substitution at the V site of PVO. Tsuchiya et al.³² synthesized $\text{PbFe}_{0.5}\text{V}_{0.5}\text{O}_3$ under high pressure and found the crystal structure as a tetragonal perovskite with $c/a = 1.18$. The magnetic study revealed that the compound is an antiferromagnet and the electrical polarization is estimated to be as large as $88 \mu\text{C}/\text{cm}^2$. Arévalo et al.³³ studied Ti and Cr substitutions at V site in PVO. A tetragonal-to-cubic transition was observed as the Cr substitution level reaches 0.4, whereas the Ti substitution preserves the $P4mm$ symmetry. The interesting result observed by Arévalo et al.³³ was the temperature-induced phase transition from tetragonal to cubic in $\text{PbTi}_{0.8}\text{V}_{0.2}\text{O}_3$ at 730 K. But PVO decomposes to $\text{Pb}_2\text{V}_2\text{O}_7$ at 570 K before reaching its transition temperature.¹⁵ In another V site, Ti-substituted PbMO_3 system (where M stands for V site substituted with Ti), Ricci³⁴ predicted multiferroicity in $\text{PbTi}_{0.875}\text{V}_{0.125}\text{O}_3$ with a ferromagnetic–ferroelectric ground state and an electrical polarization of $95 \mu\text{C}/\text{cm}^2$. Recently, Pan et al.³⁵ have experimentally studied the $\text{Pb}(\text{Ti},\text{V})\text{O}_3$ system where the V substitution level varies from 0.1 to 0.6. They have found that in the whole composition range, the $P4mm$ symmetry was preserved and the tetragonality was abnormally improved (so the spontaneous polarization) with the replacement of Ti with V. Interestingly, they have also observed an intrinsic giant volume contraction of $\sim 3.7\%$ for $\text{Pb}(\text{Ti}_{0.7}\text{V}_{0.3})\text{O}_3$ during the ferroelectric-to-paraelectric phase transition. These observed interesting findings in the substituted systems motivated us for the present study.

In the present work, we have shown that the V substitution in PTO can induce magnetism, which can lead to multiferroicity in the substituted system. Thus, our ultimate aim to design magnetoelectric materials from nonmagnetic system is satisfied. The coupling between the electric- and magnetic-order parameters is strong due to the presence of two ferroelectric mechanisms (lone pair of Pb^{2+} as well as d^0 -ness of Ti^{4+}). The 2D magnetism arises in PVO due to the d_{xy} -type orbital ordering in the ferroelectric ground state. On the other hand, the disorder induced by the substitution may release the frustration in PVO, which can lead to a long-range magnetic ordering. We hope the substitution could reduce the tendency of the system to form a 2D arrangement of V cations, which may lead to form three-dimensional (3D) magnetic ordering.

■ COMPUTATIONAL DETAILS

All of the results presented here are obtained from ab initio density functional calculations using the Vienna Ab initio Simulation Package³⁶ or full-potential linearized augmented plane-wave (FP-LAPW) method (Wien2k). To obtain the ground-state structural parameters for $\text{PbTi}_{1-x}\text{V}_x\text{O}_3$, we have optimized the crystal structure by minimizing the force and stress acting on the system. The generalized gradient approximation (GGA)³⁷ in the scheme of Perdew–Burke–Ernzerhof (PBE)³⁸ is employed to treat the exchange–correlation as it gives better equilibrium structural parameters than the local density approximation. The ionic positions and the shape of the crystals were relaxed for different unit cell volumes until the energy and force convergence criteria were reached, i.e., 10^{-6} eV per cell and 1 meV/Å per atom, respectively. As the structural parameters are very sensitive to electrical polarization, a very high plane-wave cutoff energy of 850 eV³⁹ was used. A $6 \times 6 \times 6$ Monkhorst–Pack k -point⁴⁰ mesh was used for ferroelectric PTO, and similar density of k -points was used for all other calculations. To find the ground-state magnetic ordering, we have considered nonmagnetic (NM), ferromagnetic (FM), A-type antiferromagnetic, C-type antiferromagnetic (C-AF), and G-type antiferromagnetic configurations.⁴¹ To account for the strong electron correlation associated with V 3d electrons on the electronic structure, the GGA + U method was used with $U_{\text{eff}} = 3$ eV. The Born effective charges (BECs) were calculated by the Berry phase method with a $8 \times 8 \times 8$ k -point mesh per f.u. using the modern theory of polarization.^{42,43} We have used periodic supercell approach to simulate the substituted systems, i.e., for compositions with 33 and 50% V substitutions, $1 \times 1 \times 3$ and $1 \times 1 \times 2$ supercells were created, respectively. Then, one Ti atom was replaced with V to mimic the experimental conditions. The supercells are again doubled in each direction to incorporate different magnetic orderings. Similar kind of methodology was used to model other compositions.

The orbital moments at the transition-metal sites were calculated using the orbital polarization correction (SO + OP) method implemented in Wien2k.⁴⁴ In addition, we have simulated X-ray circular magnetic dichroism (XMCD)⁴⁵ spectra using Wien2k and estimated the site-selective spin and orbital magnetic moments of V ions using the XMCD sum rules.^{46,47} For simulating XMCD, we have used full-potential linearized augmented plane-wave (FP-LAPW) method based on density functional theory as implemented in the Wien2k code. The generalized gradient approximation within the PBE scheme was used as the exchange–correlation potential. The muffin tin radii for Pb, V, and O were chosen as 1.66, 2.49, and 1.50 a.u., respectively. The Brillouin zone integration has been carried out with 5000 k -points. The energy convergence with a convergence criterion of 10^{-5} was obtained. The spin–orbit coupling is considered in the calculation. As the ferromagnetic state is a metal, the plasma frequency was first calculated and included in the XMCD calculation.

■ RESULTS AND DISCUSSION

Structural Phase Stability. PVO is a C-type antiferromagnet (see Figure 1) due to the presence of a d electron with $S = 1/2$. In oxides, it can either occur in the middle of an octahedron cage (CaVO_3 , SrVO_3)⁴⁸ or it can form a strong vanadyl bond with one O with a short bond length (ca. 1.55–1.60 Å).⁴⁹ PVO is reported to exhibit a tetragonal-to-cubic

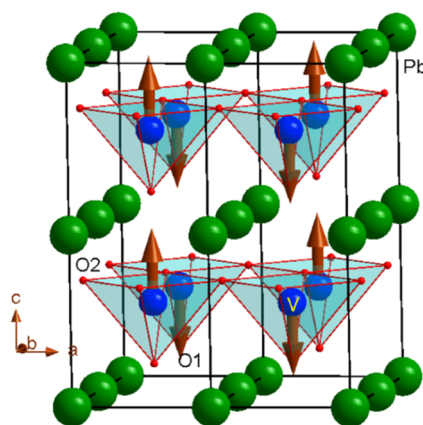


Figure 1. C-type antiferromagnetic structure of PVO. Pb and V atoms are labeled on the illustration as green (big) and blue (medium) spheres, respectively. Oxygen atoms occur at the corners of the VO_5 square pyramid and are labeled as red (small) spheres. Two types of oxygen atoms are present in PbVO_3 , one at apical (labeled as O1) and the other at the planar (labeled as O2) position. The optimized atomic positions are Pb [0, 0, 0], V [0.5, 0.5, 0.5708 (0.5677)], O1 [0, 0, 0.2128 (0.2087)], and O2 [0, 0, 0.6902 (0.6919)]. The values in parentheses are from experimental measurements.¹⁶

phase transition under pressure, but no structural transition was observed from 0 K to its decomposition temperature.¹⁶ Moreover, the minimum (apical) V–O bond length in the VO_5 pyramid in tetragonal PVO is 1.68 Å. This relatively longer bond shows a comparatively weaker vanadyl bond than usual. The average of the four planar V–O bond lengths is 1.99 Å. In agreement with these findings, the calculated Goldschmidt tolerance factor for PVO also shows a value of 1.036, which usually indicates noncentrosymmetric distortion.

Here, we have made structural optimizations for both the ferroelectric ($P4mm$) and paraelectric ($Pm\bar{3}m$) phases of $\text{PbTi}_{1-x}\text{V}_x\text{O}_3$ for $x = 0, 0.25, 0.33, 0.50, 0.67, 0.75,$ and 1 compositions. The substitution of V for Ti in PTO does not affect the symmetry of the crystal as it retains the tetragonal symmetry for the whole composition range.³⁵ With increasing V content (x), the lattice parameter c increases almost linearly and a decreases gradually, as shown in Figure 2. This results in an unusual enhancement in the tetragonality of the $\text{PbTi}_{1-x}\text{V}_x\text{O}_3$. This can be understood on the basis of ionic radii of Ti^{4+} and V^{4+} ions. The coordination number of Ti^{4+} changes from six to five with increasing concentration of vanadium. The ionic radius of V^{4+} is 0.53 Å, whereas the ionic radii of Ti^{4+} are 0.61 and 0.51 Å for sixfold and fivefold coordinations, respectively.⁵⁰ So, with decrease in ionic radii, the lattice parameter $a(b)$ decreases to accommodate the smaller cation. On the other hand, with increase of V concentration, the chance of vanadyl bond formation increases, which leads to an increase in the length of c axis. This is also the reason behind the increase in volume with the increase of x . It may be noted that PTO-modified ferroelectrics such as $(1-x)\text{PTO}-x\text{Bi}(\text{Ni}_{1/2}\text{Ti}_{1/2})\text{O}_3$ ⁵¹ and $(1-x)\text{PTO}-x\text{Bi}(\text{Mg}_{1/2}\text{Ti}_{1/2})\text{O}_3$ ⁵² usually do not show high value of c/a ratio. But some of the PTO-based compounds, i.e., $(1-x)\text{PTO}-x\text{BiFeO}_3$,⁵³ BiInO_3 –PTO,⁵⁴ and $(1-x)\text{PTO}-x\text{Bi}(\text{Zn}_{1/2}\text{Ti}_{1/2})\text{O}_3$ ⁵⁵ show abnormally high tetragonality. In the present study, the achieved maximum tetragonality (c/a) for a PTO-based compound, i.e., $\text{PbTi}_{0.25}\text{V}_{0.75}\text{O}_3$, is 1.24. This value is larger than that of some of the conventional perovskite

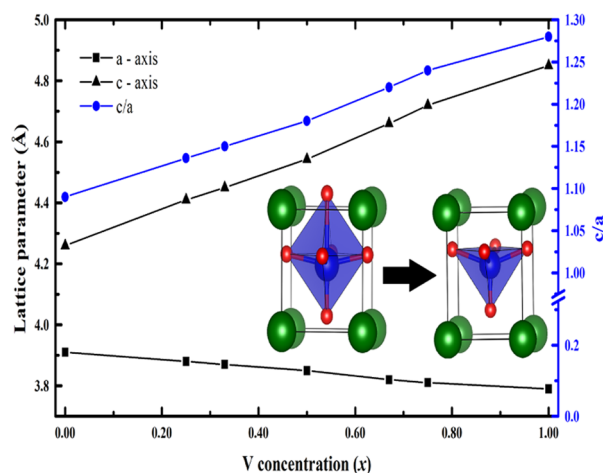


Figure 2. Evolution of lattice parameters in $\text{PbTi}_{1-x}\text{V}_x\text{O}_3$ as a function of x . The rapidly increasing c and slowly decreasing a result in unusual enhancement in c/a value. The inset shows the octahedral environment changes into pyramidal one due to increase in tetragonal distortion with increasing x .

ferroelectrics such as $0.5\text{PTO}-0.5\text{BiFeO}_3$ ($c/a = 1.14$), $0.85\text{PTO}-0.15\text{BiInO}_3$ (1.08), and $0.6\text{PTO}-0.4\text{Bi}(\text{Zn}_{1/2}\text{Ti}_{1/2})\text{O}_3$ ($c/a = 1.11$). PTO-based ferroelectric materials with large c/a possess interesting physical properties, such as high value of ferroelectric polarization (\mathbf{P}_s), high Curie temperature (T_C), and enhanced negative thermal expansion (NTE). In this study, we have shown that PTO-based material with large c/a value possesses strong magnetoelectric coupling as well as giant magnetovolume effect.

The unit cell volume is sensitive to structural transition in $\text{PbTi}_{1-x}\text{V}_x\text{O}_3$, i.e., it contracts when a ferroelectric-to-paraelectric transition takes place. For $x = 0.25$, the volume contracts by 4.2% during the phase transition. Most interestingly, the volume contraction increases with increase in V content. The volume contraction value increases to 6.3% for $x = 0.50$ and 8.4% for $x = 0.67$. When $x = 1$, the volume contracts by a value as large as 10.4% at the ferroelectric-to-paraelectric phase transition point. One of the main factors for volume contraction in this series of compounds at the phase transition is the change in bonding between Pb–O and Ti/V–O, which is discussed below. PTO-based composites with a high value of volume contraction during phase transition can give rise to interesting properties like high NTE. Moreover, a temperature-induced phase transition is observed experimentally for $x \leq 0.3$.³⁵ So, it can be said that for higher amount of Ti substitution in PbVO_3 , T_C can be measurable without decomposition.

The cubic structure of PVO can be considered as a special case of ideal tetragonal perovskite with $c/a = 1$. The ferroelectric polarization is very sensitive to structural parameters. So, to calculate the c/a ratio for various compositions accurately, we have calculated the total energy as a function of c/a . We have performed this calculation with a $1 \times 1 \times 2$ supercell, which means we should get a minimum energy for $c/a = 2$ for a cubic system. Consistent with this, our $E \sim c/a$ graph (see Figure S1 in the Supporting Information) for PVO ($x = 0$) shows a minimum energy for $c/a = 2$ for the paraelectric phase, whereas for the ferroelectric phase, we get a noninteger c/a . To find the possible polarization path, we have calculated the total energy as a function of Pb displacement with respect to V/Ti–O polyhedra. Figure 3 helps us to find

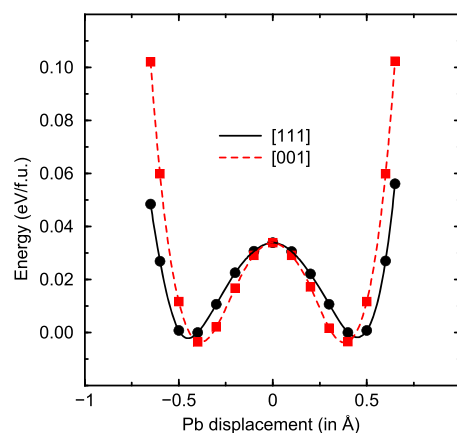


Figure 3. Total energy as a function of displacement of Pb ion along the [001] and [111] directions for the ferroelectric PVO. Structural relaxations were considered through selective dynamics.

the easiest path of the ferroelectric polarization and the role of Pb ions in the tetragonal distortion. We have plotted the displacement of Pb ion with respect to VO_5 pyramid along the [111] and [001] directions. The energy versus displacement curves for both the directions have double-well shapes. It can be seen that the lowest energy for the off-center displacements is along the [001] direction. It shows that the ferroelectric properties are greatly affected by the polarizability of Pb. The energy difference between the two directions is very small (about 2 meV/f.u.) compared to well-known multiferroic BiFeO_3 .³⁹ So, in principle, the Curie temperature of PVO must be less than that of BiFeO_3 . However, the T_C for PVO has not been estimated yet, as it decomposes before reaching to its paraelectric phase. But the T_C of $\text{PbTi}_{0.9}\text{V}_{0.1}\text{O}_3$ was estimated to be 823 K by Pan et al.,³⁵ and it showed an increasing trend V concentration (measured T_C 's for $\text{PbTi}_{0.8}\text{V}_{0.2}\text{O}_3$ and $\text{PbTi}_{0.7}\text{V}_{0.3}\text{O}_3$ are in between 823 and 873 K). Compositions with $x > 0.3$ decompose before reaching their T_C .

We have also performed nudged elastic band (NEB) calculations to find out the energetics of ferroelectric-to-paraelectric phase transition and to identify a minimum-energy path for the phase transition. To calculate the minimum-energy path, we have considered the tetragonal phase of PbVO_3 as the initial structure and the cubic phase as the tetragonal structure. Different intermediate images were created, and the energies for all of the images were calculated considering the volume as well as shape variation. The energies obtained are plotted versus the images (here mentioned as reaction coordinates). The graph given in Figure 4 results from NEB calculations, which shows that the ferroelectric-to-paraelectric transition involves an energy barrier of 127 meV, which is higher than the difference between the ground-state total energies of these two phases, i.e., ~ 70 meV. It also shows the V–O coordinated polyhedra. In the case of ferroelectric phase, the V–O polyhedron is highly distorted and makes a pyramidal arrangement. The intermediate images along the FE-to-PE transition path with higher energies than the FE phase possess comparatively less distorted polyhedra. Finally, the end product, i.e., the paraelectric phase, exhibits an undistorted octahedron. The high energy barrier for the phase transition is consistent with the high-temperature FE-to-PE phase transition.

Chemical Bonding. The chemical bonding analysis in compounds similar to PVO, i.e., BaTiO_3 and PTO, shows that

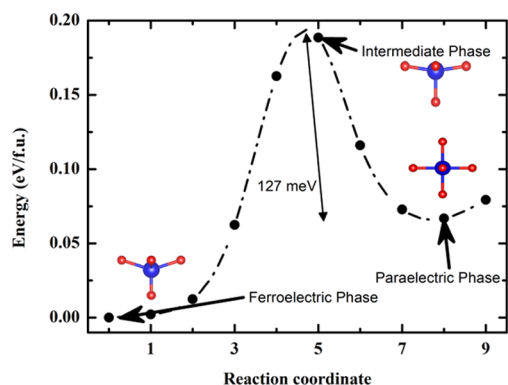


Figure 4. Ferroelectric-to-paraelectric transition path for PVO obtained from nudged elastic band method. Both volume and shape variations during the transition are considered. The insets show the V and O coordination for the particular images marked by arrows. The atom colors are the same as in Figure 1.

the ferroelectric instability arises due to the hybridization interaction between Ti 3d and O 2p states.⁵⁶ So, it is interesting to analyze the chemical bonding between V/Ti and O in $\text{PbTi}_{1-x}\text{V}_x\text{O}_3$ to reach the depth of the origin of ferroelectricity. Experimental results and theoretical analysis also show that a significant hybridization is present between Pb and O.⁵⁷ This also contributes to the Born effective charges (BEC) and, consequently, to polarization.

The charge density plot for $x = 0, 0.50,$ and 1 compositions is shown in Figure 5. It can be seen from Figure 5a–c that the charge density between the B-site cation and apical oxygen increases as the V concentration increases. In PVO, the presence of strong V–O1 bond along with lone pair electrons at the Pb^{2+} site weakens the Pb–O1 bond. Because of these effects, the Pb atom shifts more toward O2 to maintain the charge balance. Hence, the covalent bonding interaction between Pb and O2 shows an increasing trend, which is evident from Figure 5d–f as the width of the charge density increases with increase in x . These observations indicate that the increase of V concentration in $\text{PbTi}_{1-x}\text{V}_x\text{O}_3$ not only

increases the covalent bonding between Ti/V and O1 but also that between Pb and O2. As a consequence, the tetragonal distortion increases with increase in x .

The charge density plots for PVO in cubic and tetragonal phases are shown in Figure 6a (top and bottom, respectively). It can be seen that the charge density distributions at the Pb and O sites are essentially isotropic in nature for the paraelectric phase. On the other hand, a finite amount of charge can be seen in between Pb and O in the tetragonal phase showing the anisotropic nature of charge density distribution. So, it can be stated that in cubic phase, the Pb–O bond has more ionic character and the tetragonal phase has a mixed ionocovalent bonding character. On the other hand, the bonding between V and O is found to have substantial covalency in both the cubic and tetragonal phases as we can find notable charge density between these atomic sites. But it may be noted that the covalent interaction between V and O in tetragonal phase is stronger than that in the cubic phase. Due to this, the V atom is shifted from the center of the octahedron stabilizing the ferroelectric state.

Charge transfer distribution shows isotropic nature at the Pb and O sites (Figure 6b) in the cubic phase confirming the ionic bonding between Pb and O. The anisotropic nature of charge transfer distribution between V and O indicates the presence of finite covalent bonding between these atoms in the cubic phase. The charge transfer distribution between V and O as well as between Pb and O in tetragonal phase shows anisotropic behavior, as shown in Figure 6b, indicating the presence of finite covalent bonding between them. It may be noted that although the covalency between Pb and O is weaker than that between V and O in the tetragonal phase, it has equal importance in the structural and ferroelectric properties.

Electron localization function (ELF) also provides important information about the bonding interaction between the constituents of a compound. It can be seen from Figure 6c that the ELF is maximum at O sites and minimum at Pb and V sites for both the paraelectric and ferroelectric phases. Finite ELF can be seen in between V and O in the tetragonal phase showing the presence of finite covalent bonding between them.

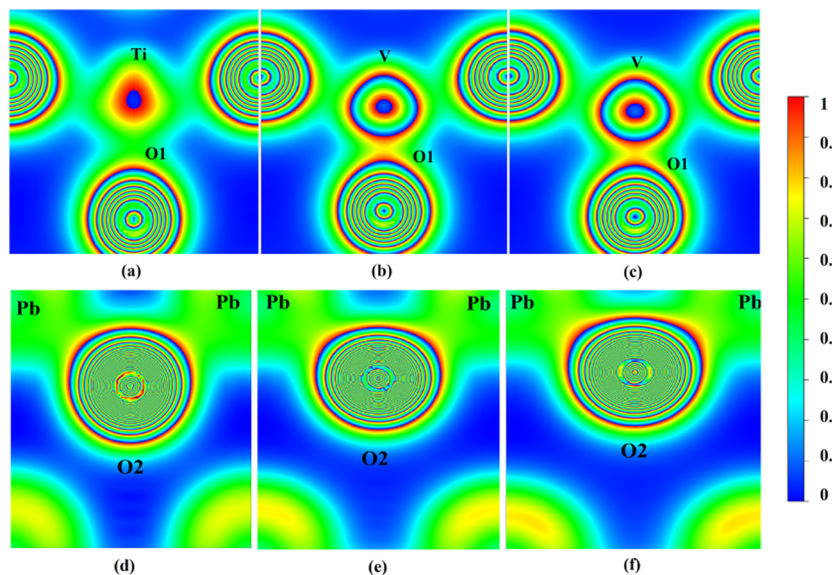


Figure 5. Charge density between (a) Ti and O1 in PbTiO_3 , (b) V and O1 in $\text{PbTi}_{0.5}\text{V}_{0.5}\text{O}_3$, (c) V and O1 bond in PbVO_3 , and (d) Pb and O2 in PbTiO_3 , (e) $\text{PbTi}_{0.5}\text{V}_{0.5}\text{O}_3$, and (f) PbVO_3 .

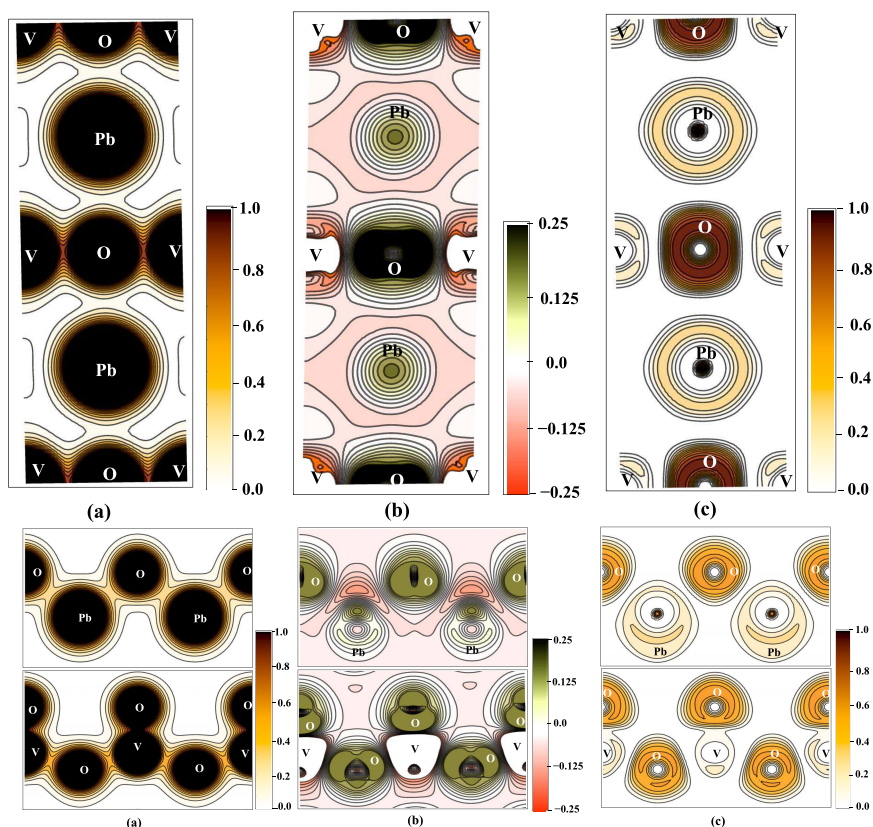


Figure 6. (a) Charge density, (b) charge transfer, and (c) electron localization function (ELF) for the paraelectric (top) and ferroelectric (bottom) structures.

The presence of the stereochemically active lone pair electrons at Pb site is also clearly visible in the ELF plot for the tetragonal case. So, the bonding interaction between Pb and O as well as between V and O in the ferroelectric tetragonal phase can be concluded as having dominant ionic character with finite covalent bonding. The difference in the bonding behaviors of Ti/V–O and Pb–O bonds for paraelectric and ferroelectric phases plays a crucial role for the large volume contraction during the ferroelectric-to-paraelectric phase transition. We have also plotted the isosurface of the valence electron localization function with an ELF value of 0.7, which is shown in Figure 7. This figure shows the lobe like lone pairs of hybridized 6s electrons at the Pb site. The charge density and charge transfer plots show that finite amount of electrons from Pb sites covalently interact with O 2p ensuring that 6s electrons of Pb are not completely chemically inert.

The site and orbital-projected densities of states (DOS) for paraelectric and ferroelectric phases for their respective ground-state magnetic configurations are shown in Figure 8a,b, respectively. It can be seen that the V 3d states and O 2p states are spread over in the valence band in a range of -7 eV to Fermi level (E_F). The energetically degenerate nature of these two states indicates the presence of strong covalent hybridization between V and O. This hybridization weakens the short-range repulsion to lower the energy of the ferroelectric phase. The filled O 2s states form narrow bands around -18 eV (see Figure 8b). Above that, at around -9 eV, the Pb 6s lone pair electronic states are present with small contributions from 2p electrons. This also confirms that the 6s electrons are stereochemically active and not inert. Although the Pb 6p states are well separated from its 6s states and are

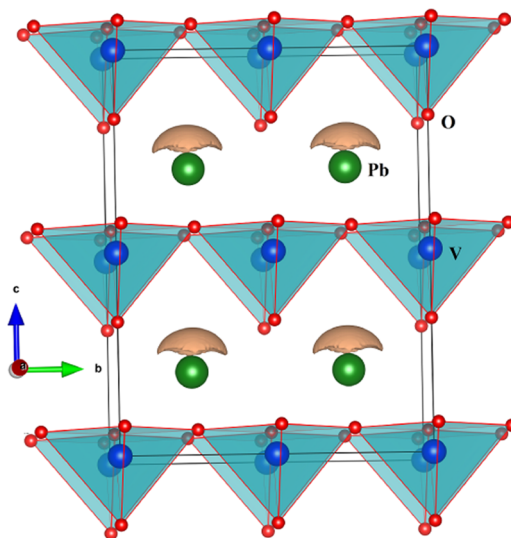


Figure 7. Valence electron localization function isosurface plotted at a value of 0.7 for PVO in the ferroelectric $P4mm$ structure.

mostly present in conduction band (CB), a small amount of Pb 6p states can be seen, which are degenerate with O 2p states confirming the Pb–O covalency. The hybridization between these states enhances the stability of the ferroelectric phase by lowering the total energy of the system. The partial DOS for $\text{PbTi}_{0.5}\text{V}_{0.5}\text{O}_3$ calculated with GGA + U ($U_{\text{eff}} = 3$ eV) is given as Figure S2 in the Supporting Information. A similar kind of DOS distribution can be seen for Pb, V, and O atoms in $\text{PbTi}_{0.5}\text{V}_{0.5}\text{O}_3$ also. The almost empty d states indicate the d^0 -

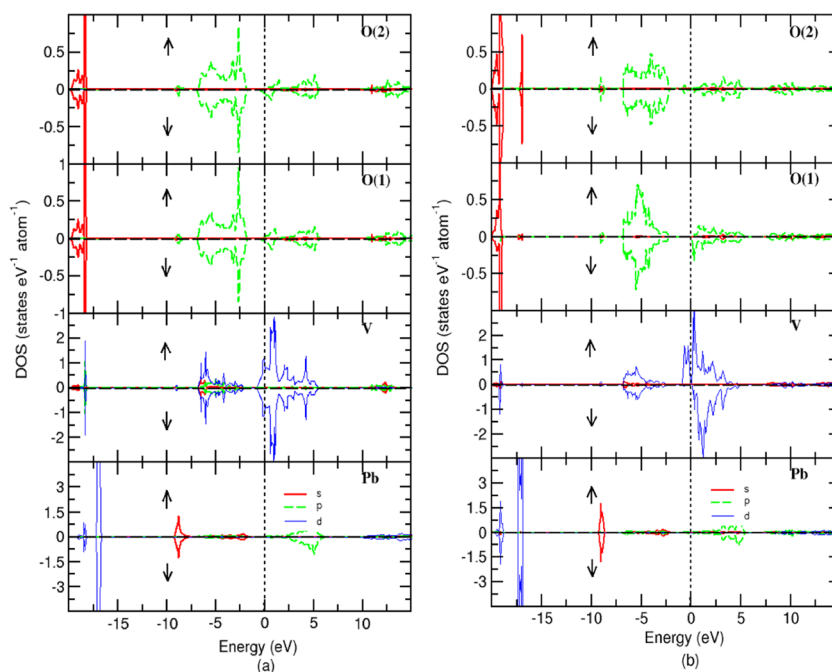


Figure 8. Site and orbital-projected density of states (DOS) for PVO for the respective ground-state magnetic structures in the (a) paraelectric and (b) ferroelectric phases. The Fermi level is set to zero.

ness of Ti^{4+} . Due to the covalent interaction between Ti and O, the charges redistribute among themselves for which we see very small yet notable DOS in Ti valence band.

The nature and strength of the bonding can also be determined by crystal orbital Hamilton population (COHP) analysis where the negative and positive COHP values indicate bonding and antibonding interactions, respectively. We have calculated the COHP among the constituents of PVO (Pb–O, Pb–O₂, V–O₁, V–O₂, O₁–O₂) as shown in Figure 9. It can be seen that all of the occupied states for Pb–O and V–O interactions have bonding states for both paraelectric and ferroelectric phases. The Pb–O₂ interaction for both the paraelectric and ferroelectric phases are almost the same. But the interaction between Pb and O₁ in the ferroelectric case has more bonding states, which are due to the hybridization between O 2p and Pb 6s/6p states. This indicates the presence of stronger covalency between Pb and O₁ in the case of the ferroelectric phase compared to the paraelectric one, which is also consistent with our charge density and partial DOS analyses. In the ferroelectric phase, the V–O₁ bonding interaction is stronger than V–O₂ bonding interaction, which is due to the off-center displacement of V atom toward the O₁ atom.

Electronic Structure. The total DOS given in Figure 10a for the paraelectric phase shows a metallic behavior for all magnetic configurations. From the total DOS of the ferroelectric phase (Figure 10b), it can be seen that the nonmagnetic phase shows a metallic state, whereas the ferromagnetic case is a half metal with a gap of ~ 0.5 eV in the down-spin channel. But when the antiferromagnetic ordering is introduced, the exchange potential produced by the exchange interaction pushes the V 3d states toward the lower-energy side, which results in an insulating state with a narrow gap. So, a combination of spin polarization, magnetic ordering, and crystal structure plays important roles in stabilizing the ferroelectric phase of PVO. The broad band spreading from -7 to -2 eV is mainly due to the strong

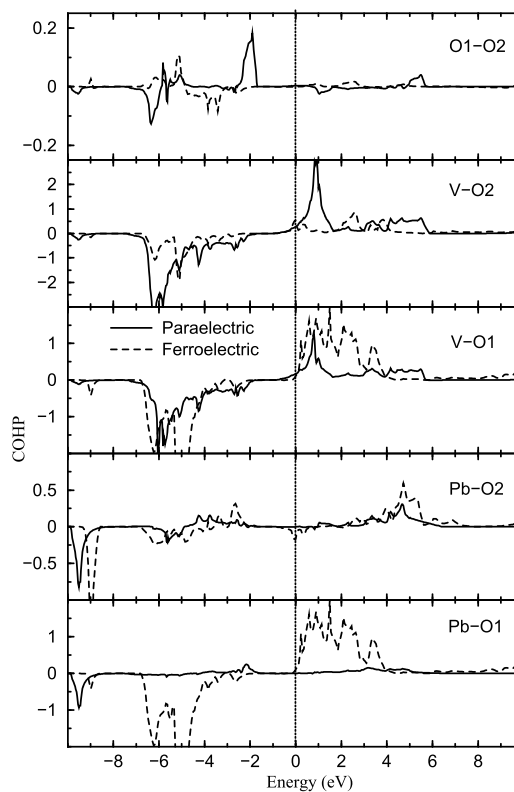


Figure 9. Crystal orbital Hamilton population (COHP) for PVO in the paraelectric and ferroelectric phases describing Pb–O, Pb–O₂, V–O₁, V–O₂, O₁–O₂. O₁ and O₂ are the planar and apical oxygen atoms, respectively.

hybridization between V 3d and O 2p electrons. The localized states at around -9 eV are generated from the hybridized Pb 6s lone pair electrons. After including the correlation effect through the Hubbard U into the Hamiltonian matrix, the states

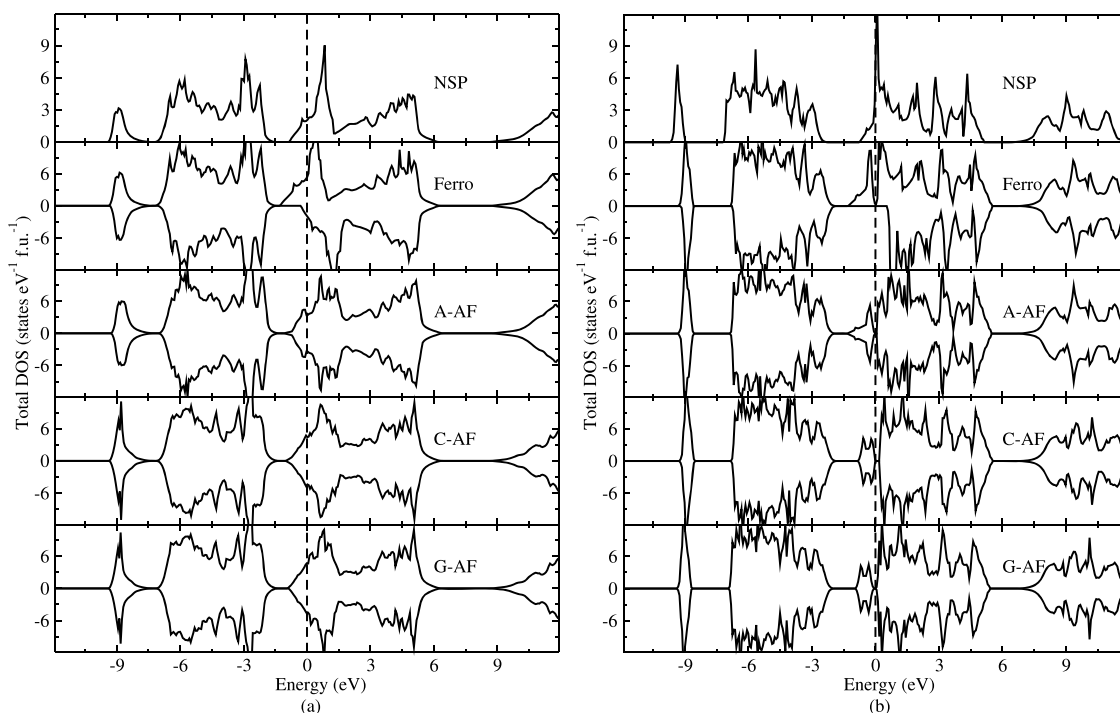


Figure 10. Total density of states for PVO in the non-spin-polarized, ferromagnetic, A-, C-, and G-type antiferromagnetic configurations for (a) paraelectric and (b) ferroelectric phases. The Fermi level is set to zero.

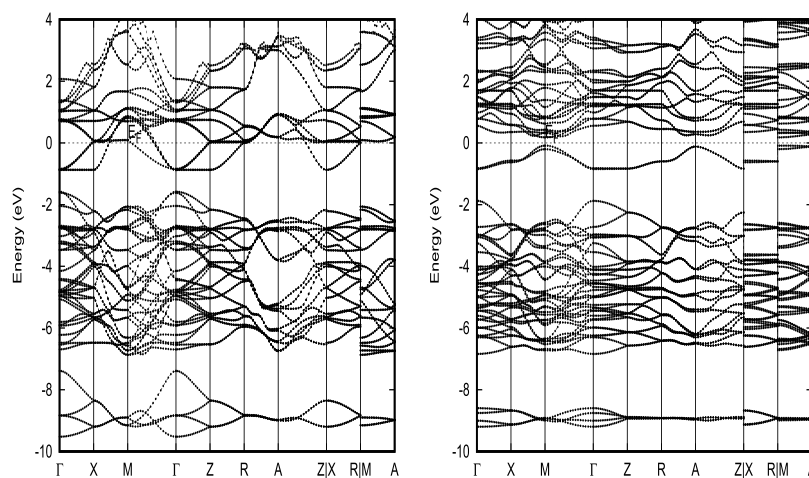


Figure 11. Electronic band dispersion for PVO in the (left) paraelectric and (right) ferroelectric phases. The Fermi level is set to zero.

get more localized to give a larger band gap, and this localization of the d electrons produces a larger magnetic moment.

The total DOS for $x = 0.33$, 0.50 , and 0.67 compositions were calculated with the GGA + U method, as shown in Figure S3 in the Supporting Information. The band gap value decreases with increase in x . As it is known that the bond lengths and lattice parameters have direct impact on band gaps, the decreasing band gap may be attributed to the increase in the average Ti/V–O bond length with x in Ti/V–O₆ polyhedra. (The average Ti–O bond length is 2.07 \AA in PTO, whereas the V–O bond length is 2.11 \AA in the case of PVO.) The lattice parameter c also increases with x .

The band structures for both the para- and ferroelectric phases of $x = 1$ composition are shown in Figure 11. The k -path considered in the band structure is shown in Figure S4 in

the Supporting Information. The lowest bands seen around 9 eV below the E_F are due to the Pb 6s states. It is to be noted that these bands are broader in the paraelectric phase, whereas in the ferroelectric phase, they are more localized in a small energy range. This explains the effect of 6s lone pair in stabilizing the ferroelectric state. A manifold of occupied O 2p bands are spread over a range of -7 to -2 eV . A pair of bands separated from O 2p bands are localized just below E_F . These are having V 3d character with no dispersion along Γ –Z direction and a very weak dispersion along X–R as well as M–A directions indicating a 2D characteristic in the ab plane.¹⁸ Above these band features, a narrow gap with the value of 0.2 eV is present in the ferroelectric phase. The conduction bands located in the vicinity of CB edge are derived from V 3d states, but the bands at higher energy ($\sim 3 \text{ eV}$) have mainly Pb 6p character. We have also calculated the band structure with the

GGA + U method. The GGA + U band structures for $x = 0.5$ and 1 compositions are given in Figures S5 and S6 in the Supporting Information. It can be seen that when the V concentration is low, the vanadyl bond weakens and therefore the d_{xy} band gets dispersed along the Γ -Z, X-R, and M-A directions. This indicates that the tendency of the system to form the 2D magnetism is reduced for lower x values.

Magnetic Properties. We have calculated total energies for nonmagnetic and all of the magnetic orderings mentioned above for $\text{PbTi}_{1-x}\text{V}_x\text{O}_3$ in both paraelectric and ferroelectric phases, as shown in Table S1 in the Supporting Information. PTO is a well-known nonmagnetic compound. Our total energy calculation reveals that the C-AF is the ground state for other compositions. It is to be noted that the C-AF and G-AF states are almost degenerate (see Table S1 in the Supporting Information). The present observation of C-AF state as a magnetic ground state for PVO is consistent with experimental observation of a two-dimensional C-AF phase and also with other theoretical studies.^{14,17} To identify the exact composition where the nonmagnetic-to-magnetic transition occurs, we have plotted ΔE versus x (where $\Delta E = E_{\text{C-AF}} - E_{\text{NM}}$) for the ferroelectric phase, as shown in Figure S7 in the Supporting Information. The energy difference increases linearly as the concentration of V increases due to the increase in localized d electrons density per cell making the antiferromagnetic state more stable. We have extrapolated the ΔE versus x curve, and the magnetic transition point is found to be $x \sim 0.123$. This is in agreement with previous theoretical finding by Ricci et al.³⁴ using similar calculations that the magnetic ground state stabilizes in $\text{PbTi}_{1-x}\text{V}_x\text{O}_3$ for $x = 12.5\%$.

The total energy shows a nonmagnetic ground state for the paraelectric phase of $\text{PbTi}_{1-x}\text{V}_x\text{O}_3$. So, the ferroelectric-to-paraelectric phase transition is associated with a magnetic-to-nonmagnetic transition, which shows a strong coupling between the electric and magnetic-order parameters for $x > 0.123$. Now, the large values of volume contraction during the structural transition can also be attributed to the associated magnetic phase transition. So, it can be said that this series of compounds possess not only giant magnetoelectric effect but also giant magnetovolume effect. It is to be noted that compounds with strong magnetovolume effect can be used to convert magnetic energy into kinetic energy or vice versa and are used to build actuators and sensors.

The orbital-projected DOS for the V 3d electrons for both paraelectric and ferroelectric phases in PVO are given in Figure 12a,b, respectively. In the presence of a cubic octahedral crystal field, the d level of transition-metal cation splits into t_{2g} (with degenerate d_{xy} , d_{yz} , and d_{zx} orbitals) and e_g (with degenerate $d_{x^2-y^2}$ and d_{z^2}) orbitals. The e_g levels are completely empty, whereas the t_{2g} states are partially filled in the paraelectric phase resulting in a metallic state. The ferroelectric phase of PVO has a square pyramidal coordination (Figure 1) because of the off-center displacement of V. Due to the presence of VO_5 square pyramidal environment, the t_{2g} level of V 3d electrons splits into b_{2g} (d_{xy}) and doubly degenerate e_g (d_{yz} , d_{zx}) levels with an energy difference of ~ 1 eV. Similarly, the degeneracy of e_g level breaks to produce separate b_{1g} ($d_{x^2-y^2}$) and a_{1g} (d_{z^2}) levels.²⁴ The orbital degeneracy is broken because of the second-order Jahn–Teller ordering. This was also noted in the YTiO_3 with d^1 configuration of Ti^{3+} similar to V^{4+} in our study.⁵⁸ The orbital-projected DOS for the ferroelectric phase given in Figure 12b shows that the localized V 3d electrons are present in the lowest-lying d_{xy} orbital, which is separated from

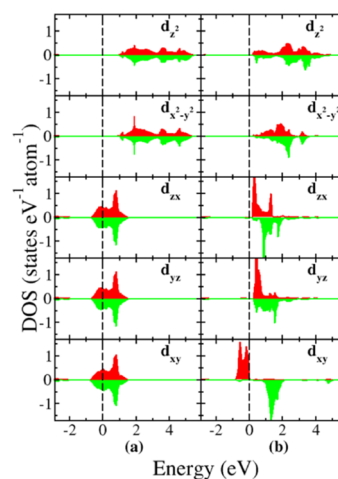


Figure 12. Orbital-projected density of states for the 3d electrons in the V site of PbVO_3 in the (a) paraelectric and (b) ferroelectric phases for their respective ground-state magnetic structures. The Fermi level is set to zero.

other d orbitals by crystal field splitting, making a spin 1/2 antiferromagnetic ordering in the ab plane. Due to the localized nature of this d-electron, there is a strong intraatomic exchange splitting that shifts the unoccupied d_{xy} states to relatively higher energy.

We know that the electrons present in the vicinity of Fermi level actively participate in electrical conduction and magnetic exchange interactions. So we have used the integrated values of the orbital-projected DOS, i.e., from E_F to -1 eV, to study the orbital ordering. We have used the same procedure for OO study as given in our previous studies,^{59,60} and such analysis provides not only the OO pattern but also a pictorial illustration of the orientation of a particular d orbital. The OO patterns for ferroelectric and paraelectric phases are shown in Figure 13. It can be seen that the V atom has a d_{xy} pattern OO in the ferroelectric phase. This type of orbital ordering in PVO strengthens the intraplanar V–O–V interactions and also stabilizes the 2D magnetism. Hence, the magnetic and orbital ordering are ingeniously coupled with the lattice distortion and ionic displacements that result in strong magnetoelectric coupling. But in the cubic paraelectric case, the V–O–V interactions are strong enough to create an itinerant-electron band with all of the t_{2g} orbitals partially filled. So, the OO pattern for paraelectric phase does not show a particular manner of ordering from any of the t_{2g} orbitals. This weakens the exchange coupling and stabilizes a nonmagnetic ground state.

The calculated magnetic moment at the V site is $0.93 \mu_B$ for the ferroelectric phase. The covalency present between V and O induces a magnetic moment of $0.05 \mu_B$ at the O site. The orbital magnetic moment at the V site evaluated using the SO + OP method is estimated to be $-0.045 \mu_B$. This indicates that the orbital magnetic moment is aligned antiparallely with the spin magnetic moment. The magnitude of the orbital moment of PVO is almost 5 times less than that of BiCoO_3 .⁶¹ This is due to the presence of relatively larger spin moment and stronger spin–orbit coupling in BiCoO_3 .

We have calculated the magnetic anisotropy energy^{62,63} for $x = 0.5$ and 1 in their ground-state C-AF configurations. For this, we have calculated the variation of total energy by changing the direction of the magnetization with the force theorem for the

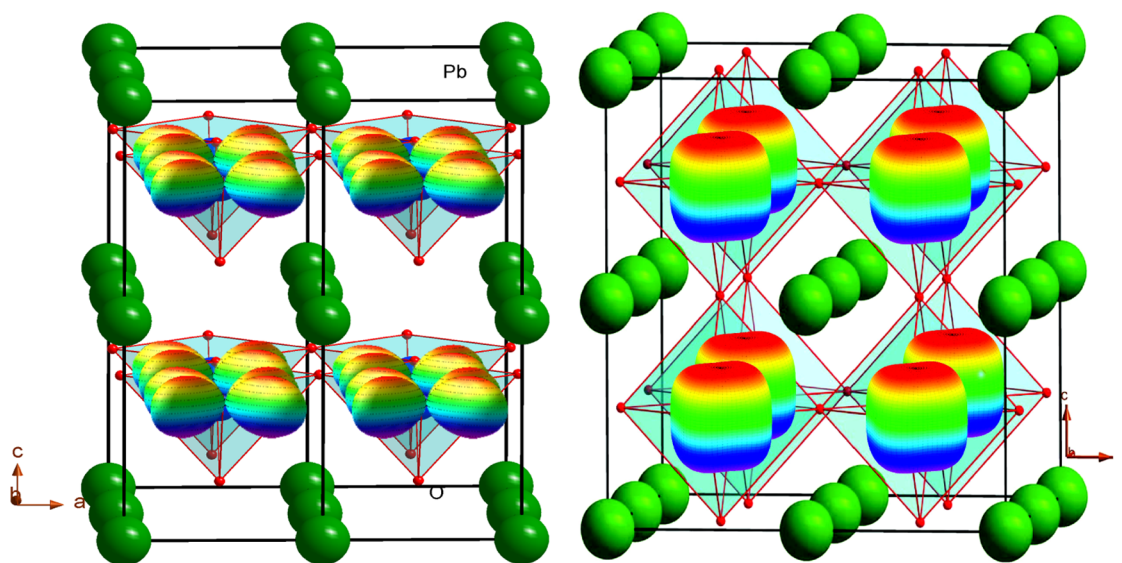


Figure 13. Orbital ordering pattern of PVO in (left) the ferroelectric and (right) paraelectric phases as derived from full-potential calculations.

compositions $x = 0.5$ and 1. The calculated relative magneto anisotropy energies for $x = 0.5$ with respect to the easy axis are 0, 0.125, 0.070, and 0.048 meV/f.u. and 0.592, 1.630, 0, and 0.185 meV/f.u. for $x = 1$ in the [001], [100], [110], and [111] directions, respectively. Therefore, the easy axis for $\text{PbTi}_{0.5}\text{V}_{0.5}\text{O}_3$ and PVO are [001] and [110], respectively. The change in magnetic easy axis from $x = 0.5$ to 1 can be attributed to the formation of vanadyl bond with increase in V concentration, i.e., the $x = 0.5$ composition is a BiCoO_3 like C-AF (so it shows similar easy axis), and with increase in V concentration, the tendency to form a 2D antiferromagnetism increases (which also reflects in our band structure).

To get deeper understanding of the magnetic properties of PVO, we have simulated the XMCD and X-ray absorption spectra (XAS) at the $L_{2,3}$ edges of V in the ferromagnetic configuration of PVO. The XMCD and XAS spectra along with the left- and right-polarized spectra for V atom in PVO are given in Figure 14. By applying the sum rules^{46,47} given in the Supporting Information, we have evaluated the spin and orbital moments at the V site. The obtained orbital moment of

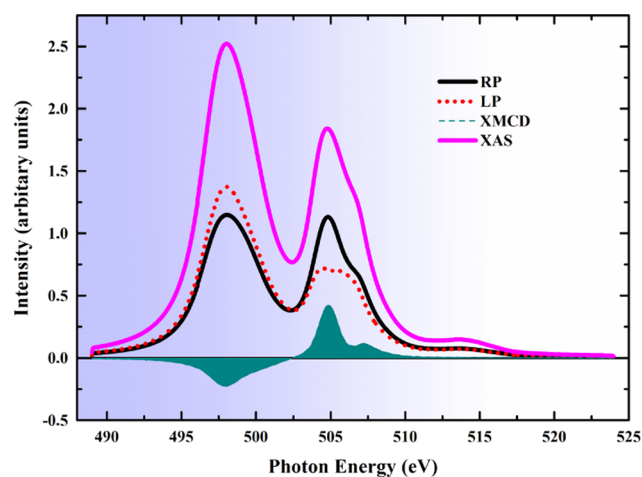


Figure 14. Absorption spectra at the V $L_{2,3}$ edges for right circular and left circular polarization of the exciting X-rays, X-ray magnetic circular dichroism, and X-ray absorption spectra in PVO.

$-0.039 \mu_B$ for V is consistent with that obtained directly from the self-consistent calculations ($-0.045 \mu_B$). The sum rule analysis results in a spin moment of $0.8 \mu_B/V$ for the V $L_{2,3}$ edges. However, this varies notably from the value calculated by the self-consistent field (SCF) method, which is $\sim 1 \mu_B/V$. Detailed analysis on different 3d compounds by Wende et al.⁶⁴ shows that the deviation of the sum rule results from the SCF predictions is larger for lighter 3d elements^{65–67} as integral sum rule analysis ignores the spectral shape of the XMCD. So, the detailed fine structure in the XMCD of V should be fitted with the multipole moment analysis, as explained in ref 67.

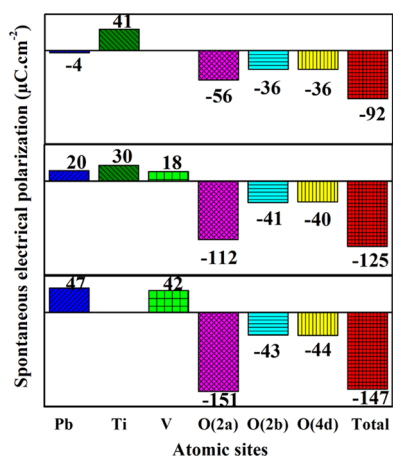
Born Effective Charge and Spontaneous Polarization.

We have calculated BECs for all of the compositions mentioned above. The diagonal components of the BECs for $x = 0, 0.5$, and 1.0 compositions are given in Table 1. The formal valences for Pb, V, Ti, and O in $\text{PbTi}_{1-x}\text{V}_x\text{O}_3$ are +2, +4, +4, and -2 , respectively. But the diagonal components of the calculated BEC tensors for the atoms are much larger than their nominal ionic values. This reveals that there is large dynamic contribution superimposed to the static charge. This is due to the strong covalency effect, where a large amount of nonrigid delocalized charge flows across this compound during the ionic displacement. This results in additional charges with respect to the nominal ionic values (anomalous contribution), which are obtained at the atomic sites. A large BEC value at the oxygen site also suggests that a large force can be generated by applying a small field which can stabilize the polarized state. In an effort to shed light on the polarization of $\text{PbTi}_{1-x}\text{V}_x\text{O}_3$ and its origin, we have evaluated the polarization of $\text{PbTi}_{1-x}\text{V}_x\text{O}_3$ for $x = 0-1$. PTO and PVO are well-studied ferroelectrics with polarization values of 92 and $147 \mu\text{C}/\text{cm}^2$, respectively. The calculated polarization values increase from $92 \mu\text{C}/\text{cm}^2$ for pure PTO to 105, 110, 118, 130, 135, and $147 \mu\text{C}/\text{cm}^2$ for $x = 0.25, 0.33, 0.5, 0.67, 0.75$, and 1, respectively. This is due to the increase in tetragonal distortion with x as discussed above. The polarization calculated with point charges showed comparatively low values. The reduction in polarization values using point charges indicates that the covalency effect plays an important role in deciding the polarization of these materials.

Table 1. Calculated Diagonal Components of the Born Effective Charge Tensors for $x = 0, 0.5,$ and 1 of $\text{PbTi}_{1-x}\text{V}_x\text{O}_3$ in the Ferroelectric Phase with Ground-State Magnetic Ordering

| $x \rightarrow$ | 0 | | | 0.5 | | | 1 | | |
|-----------------|--------|--------|--------|--------|--------|--------|--------|--------|--------|
| atom | xx | yy | zz | xx | yy | zz | xx | yy | zz |
| Pb | 3.641 | 3.641 | 3.331 | 3.623 | 3.617 | 3.664 | 3.251 | 3.232 | 3.275 |
| Ti | 6.166 | 6.166 | 4.961 | 5.480 | 5.406 | 4.778 | | | |
| V | | | | 4.348 | 4.440 | 4.435 | 4.880 | 4.824 | 3.749 |
| O1 | -1.938 | -1.938 | -4.245 | -1.148 | -1.154 | -3.098 | -1.442 | -1.525 | -3.720 |
| O2 | -2.603 | -5.266 | -2.024 | -2.078 | -3.875 | -1.417 | -2.209 | -4.029 | -1.764 |
| O3 | -5.266 | -2.603 | -2.024 | -3.716 | -1.899 | -1.423 | -3.877 | -2.513 | -1.724 |

The atom-decomposed spontaneous polarization is given for $x = 0, 0.5,$ and 1 compositions in Figure 15. The major

**Figure 15.** Calculated site-projected spontaneous electric polarization of $\text{PbTi}_{1-x}\text{V}_x\text{O}_3$ for $x = 0$ (top), 0.5 (middle), and 1 (bottom).

contribution toward the polarization is coming from the displacement of the O atom from its centrosymmetric position. It can be seen that the polarization contribution of Ti toward higher x value decreases. In contrast, an opposite trend is seen for V atom. This is because of the enhancement of covalency between B-site cation and O with V substitution at Ti site.

CONCLUSIONS

$\text{PbTi}_{1-x}\text{V}_x\text{O}_3$ possesses strong coupling between magnetic- and electric-order parameters for V concentration $> 12.3\%$. Lower substituted compositions are nonmagnetic ferroelectrics. Also, from the other side, the inclusion of Ti at the V site increases the chance of forming a 3D arrangement of V cations rather than 2D. The strong covalency between Ti/V and O and notable covalency between Pb and O bring the non-centrosymmetric distortion and stabilize the ferroelectric ground state. The ferroelectric-to-paraelectric transition is accompanied by a magnetic-to-nonmagnetic transition for $x > 0.123$. There is a large volume contraction during the above transition, indicating a strong lattice–ferroelectric coupling and strong magnetovolume effect. The calculations show high values of spontaneous electrical polarizations, which are mainly due to the displacement of the apical oxygen in the BO_6 octahedra in the paraelectric phase due to strong Ti/V–O covalent interaction. Therefore, $\text{PbTi}_{1-x}\text{V}_x\text{O}_3$ is a series of multifunctional compounds having giant magnetoelectric effect where one can change the magnetic properties drastically (even from magnetic to nonmagnetic, as shown here) by applying electric field and vice versa, strong magnetovolume

effect, induce 2D magnetism as well as orbital ordering by electric field, strong ferroelectric–lattice coupling, etc. Also, recent experimental studies by Pan et al.³⁵ show that for lower V concentration, this series shows good NTE response, and also a temperature-induced tetragonal-to-cubic transition occurs, which makes this series more interesting for the researchers to investigate its magneto/electro/multiferroic properties. With all of these properties coexisting in the series, $\text{PbTi}_{1-x}\text{V}_x\text{O}_3$ can be useful for many multifunctional device applications.

ASSOCIATED CONTENT

Supporting Information

The Supporting Information is available free of charge on the ACS Publications website at DOI: 10.1021/acsomega.9b01176.

Energy vs c/a ratio curves, partial DOS for $x = 0.50$ with the GGA + U method, total DOS for $x = 0.33, 0.50,$ and 0.67 with the GGA + U method, the Brillouin zone path used for band calculations, electronic band structure for $x = 0.50$ with the GGA + U method, electronic band structure for $x = 1$ with the GGA + U method, variation of energy difference between magnetic and nonmagnetic states with x , and sum rule analysis (PDF)

AUTHOR INFORMATION

Corresponding Author

*E-mail: raviphy@cutn.ac.in. Tel: +91 94890 54267.

ORCID

Lokanath Patra: 0000-0002-1050-5665

Ravindran Vidya: 0000-0002-7798-1797

Helmer Fjellvåg: 0000-0001-6045-7211

Ponniah Ravindran: 0000-0003-4611-011X

Notes

The authors declare no competing financial interest.

ACKNOWLEDGMENTS

The authors are grateful to the Research Council of Norway for computing facilities (under project number NN2875k) at the Norwegian supercomputer consortium (NOTUR). This research was supported by the Indo-Norwegian Cooperative Program (INCP) via Grant No. F. 58-12/2014(IC). L.P. thanks Prof. Anja Olafsen Sjøstad for her fruitful discussions. L.P. also thanks M.R. Ashwin Kishore and A. Krishnamoorthy for critical reading of the manuscript.

REFERENCES

- (1) Fiebig, M. Revival of the magnetoelectric effect. *J. Phys. D: Appl. Phys.* **2005**, *38*, R123.

- (2) Spaldin, N. A.; Fiebig, M. The renaissance of magnetoelectric multiferroics. *Science* **2005**, *309*, 391–392.
- (3) Cheong, S.-W.; Mostovoy, M. Multiferroics: a magnetic twist for ferroelectricity. *Nat. Mater.* **2007**, *6*, 13–20.
- (4) Ramesh, R.; Spaldin, N. A. Multiferroics: progress and prospects in thin films. *Nat. Mater.* **2007**, *6*, 21–29.
- (5) Bibes, M.; Barthélémy, A. Multiferroics: Towards a magneto-electric memory. *Nat. Mater.* **2008**, *7*, 425–426.
- (6) González-Vázquez, O.; Wojdel, J. C.; Diéguez, O.; Íñiguez, J. First-principles investigation of the structural phases and enhanced response properties of the BiFeO₃-LaFeO₃ multiferroic solid solution. *Phys. Rev. B* **2012**, *85*, No. 064119.
- (7) Ma, Z.; Tian, Z.; Li, J.; Wang, C.; Huo, S.; Duan, H.; Yuan, S. Enhanced polarization and magnetization in multiferroic (1-x)-BiFeO₃-xSrTiO₃ solid solution. *Solid State Sci.* **2011**, *13*, 2196–2200.
- (8) Zhu, W.-M.; Guo, H.-Y.; Ye, Z.-G. Structural and magnetic characterization of multiferroic (BiFeO₃)_{1-x}(PbTiO₃)_x solid solutions. *Phys. Rev. B* **2008**, *78*, No. 014401.
- (9) Diéguez, O.; Íñiguez, J. First-Principles Investigation of Morphotropic Transitions and Phase-Change Functional Responses in BiFeO₃-BiCoO₃ Multiferroic Solid Solutions. *Phys. Rev. Lett.* **2011**, *107*, No. 057601.
- (10) Singh, A.; Chatterjee, R. Magnetization induced dielectric anomaly in multiferroic LaFeO₃-PbTiO₃ solid solution. *Appl. Phys. Lett.* **2008**, *93*, No. 182908.
- (11) Hang, Q.; Xing, Z.; Zhu, X.; Yu, M.; Song, Y.; Zhu, J.; Liu, Z. Dielectric properties and related ferroelectric domain configurations in multiferroic BiFeO₃-BaTiO₃ solid solutions. *Ceram. Int.* **2012**, *38*, S411–S414.
- (12) Patra, L.; Pan, Z.; Chen, J.; Azuma, M.; Ravindran, P. Metamagnetism stabilized giant magnetoelectric coupling in ferroelectric xBaTiO₃-(1-x)BiCoO₃ solid solution. *Phys. Chem. Chem. Phys.* **2018**, *20*, 7021–7032.
- (13) Chen, J.; Hu, L.; Deng, J.; Xing, X. Negative thermal expansion in functional materials: controllable thermal expansion by chemical modifications. *Chem. Soc. Rev.* **2015**, *44*, 3522–3567.
- (14) Shpanchenko, R. V.; Chernaya, V. V.; Tsirlin, A. A.; Chizhov, P. S.; Sklovsky, D. E.; Antipov, E. V.; Khlybov, E. P.; Pomjakushin, V.; Balagurov, A. M.; Medvedeva, J. E.; Kaul, E. E.; Geibel, C. Synthesis, structure, and properties of new perovskite PbVO₃. *Chem. Mater.* **2004**, *16*, 3267–3273.
- (15) Okos, A. Synthesis and Characterization of Pb(V_{1-x}M_x)O₃ Compounds. Ph.D. thesis, Université de Grenoble, 2014.
- (16) Belik, A. A.; Azuma, M.; Saito, T.; Shimakawa, Y.; Takano, M. Crystallographic features and tetragonal phase stability of PbVO₃, a new member of PbTiO₃ family. *Chem. Mater.* **2005**, *17*, 269–273.
- (17) Uratani, Y.; Shishidou, T.; Oguchi, T. First-principles study on the magnetic anisotropy in multiferroic PbVO₃ and BiCoO₃. *J. Phys. Soc. Jpn.* **2009**, *78*, No. 084709.
- (18) Singh, D. J. Electronic structure and bond competition in the polar magnet PbVO₃. *Phys. Rev. B* **2006**, *73*, No. 094102.
- (19) Tsirlin, A. A.; Belik, A. A.; Shpanchenko, R. V.; Antipov, E. V.; Takayama-Muromachi, E.; Rosner, H. Frustrated spin-1/2 square lattice in the layered perovskite PbVO₃. *Phys. Rev. B* **2008**, *77*, No. 092402.
- (20) Oka, K.; Yamada, I.; Azuma, M.; Takeshita, S.; Satoh, K. H.; Koda, A.; Kadono, R.; Takano, M.; Shimakawa, Y. Magnetic ground-state of perovskite PbVO₃ with large tetragonal distortion. *Inorg. Chem.* **2008**, *47*, 7355–7359.
- (21) Martin, L. W.; Zhan, Q.; Suzuki, Y.; Ramesh, R.; Chi, M.; Browning, N.; Mizoguchi, T.; Kreisel, J. Growth and structure of PbVO₃ thin films. *Appl. Phys. Lett.* **2007**, *90*, No. 062903.
- (22) Kumar, A.; Martin, L. W.; Denev, S.; Kortright, J. B.; Suzuki, Y.; Ramesh, R.; Gopalan, V. Polar and magnetic properties of PbVO₃ thin films. *Phys. Rev. B* **2007**, *75*, No. 060101.
- (23) Chi, M.; Mizoguchi, T.; Martin, L.; Ramesh, R.; Browning, N. Studying Thin-film Perovskite Vanadates by EELS. *Microsc. Microanal.* **2007**, *13*, 1234–1235.
- (24) Solovyev, I. Magnetic structure of the noncentrosymmetric perovskites PbVO₃ and BiCoO₃: Theoretical analysis. *Phys. Rev. B* **2012**, *85*, No. 054420.
- (25) Parveen, A.; Srivastava, A.; Gaur, N. Thermal properties of a novel compound PbVO₃. *J. Phys.: Conf. Ser.* **2012**, *377*, No. 012059.
- (26) Ming, X.; Yin, J.-W.; Wang, X.-L.; Wang, C.-Z.; Huang, Z.-F.; Chen, G. First-principles comparative study of multiferroic compound PbVO₃. *Solid State Sci.* **2010**, *12*, 938–945.
- (27) Zhou, W.; Tan, D.; Xiao, W.; Song, M.; Chen, M.; Xiong, X.; Xu, J. Structural properties of PbVO₃ perovskites under hydrostatic pressure conditions up to 10.6 GPa. *J. Phys.: Condens. Matter* **2012**, *24*, No. 435403.
- (28) Milošević, A. S.; Lalić, M. V.; Popović, Z. S.; Vukajlović, F. R. An ab initio study of electronic structure and optical properties of multiferroic perovskites PbVO₃ and BiCoO₃. *Opt. Mater.* **2013**, *35*, 1765–1771.
- (29) Ming, X.; Hu, F.; Du, F.; Wei, Y.-J.; Chen, G. First-principles study of multiferroic material PbVO₃ under uniaxial pressure. *Eur. Phys. J. B* **2015**, *88*, 212.
- (30) Kadiri, A.; Arejda, M.; Abbassi, A.; El Amraoui, Y.; Ez-Zahraoui, H.; Benyoussef, A. Calculated Magnetic Properties of the Compound PbVO₃. *J. Supercond. Novel Magn.* **2017**, *30*, 2247–2253.
- (31) Oka, K.; Yamauchi, T.; Kanungo, S.; Shimazu, T.; Oh-ishi, K.; Uwatoko, Y.; Azuma, M.; Saha-Dasgupta, T. Experimental and Theoretical Studies of the Metallic Conductivity in Cubic PbVO₃ under High Pressure. *J. Phys. Soc. Jpn.* **2018**, *87*, No. 024801.
- (32) Tsuchiya, T.; Katsumata, T.; Ohba, T.; Inaguma, Y. High-pressure synthesis and characterization of a novel perovskite PbFe_{1/2}V_{1/2}O₃. *J. Ceram. Soc. Jpn.* **2009**, *117*, 102–105.
- (33) Arévalo-López, A. M.; Alario-Franco, M. A. Structural Percolation in the PbMO_{1-x}MO_xO₃ (M, M = Ti, Cr, and V) Perovskites. *Inorg. Chem.* **2011**, *50*, 7136–7141.
- (34) Ricci, F.; Fiorentini, V. Multiferroicity in V-doped PbTiO₃. *J. Phys.: Conf. Ser.* **2013**, *470*, No. 012013.
- (35) Pan, Z.; et al. Colossal Volume Contraction in Strong Polar Perovskites of Pb(Ti,V)O₃. *J. Am. Chem. Soc.* **2017**, *139*, 14865–14868.
- (36) Kresse, G.; Furthmüller, J. Efficient iterative schemes for ab initio total-energy calculations using a plane-wave basis set. *Phys. Rev. B: Condens. Matter Mater. Phys.* **1996**, *54*, 11169–11186.
- (37) Perdew, J. P.; Burke, K.; Ernzerhof, M. Generalized gradient approximation made simple. *Phys. Rev. Lett.* **1996**, *77*, 3865.
- (38) Ernzerhof, M.; Scuseria, G. E. Assessment of the Perdew-Burke-Ernzerhof exchange-correlation functional. *J. Chem. Phys.* **1999**, *110*, 5029–5036.
- (39) Ravindran, P.; Vidya, R.; Kjekshus, A.; Fjellvåg, H.; Eriksson, O. Theoretical investigation of magnetoelectric behavior in BiFeO₃. *Phys. Rev. B* **2006**, *74*, No. 224412.
- (40) Monkhorst, H. J.; Pack, J. D. Special points for Brillouin-zone integrations. *Phys. Rev. B* **1976**, *13*, 5188.
- (41) Patra, L.; Kishore, M. A.; Vidya, R.; Sjøstad, A. O.; Fjellvåg, H.; Ravindran, P. Electronic and Magnetic Structures of Hole Doped Trilayer La_{4-x}Sr_xNi₃O₈ from First-Principles Calculations. *Inorg. Chem.* **2016**, *55*, 11898–11907.
- (42) Resta, R. Macroscopic polarization in crystalline dielectrics: the geometric phase approach. *Rev. Mod. Phys.* **1994**, *66*, 899.
- (43) King-Smith, R.; Vanderbilt, D. Theory of polarization of crystalline solids. *Phys. Rev. B* **1993**, *47*, 1651.
- (44) Blaha, P.; Schwarz, K.; Madsen, G. K.; Kvasnicka, D.; Luitz, J. In *WIEN2k: An Augmented Plane Wave Plus Local Orbitals Program for Calculating Crystal Properties*; Schwarz, K., Ed.; Vienna University of Technology: Austria, 2001.
- (45) Erskine, J.; Stern, E. Calculation of the M₂₃ magneto-optical absorption spectrum of ferromagnetic nickel. *Phys. Rev. B* **1975**, *12*, 5016.
- (46) Carra, P.; Thole, B.; Altarelli, M.; Wang, X. X-ray circular dichroism and local magnetic fields. *Phys. Rev. Lett.* **1993**, *70*, 694.

(47) Thole, B.; Carra, P.; Sette, F.; van der Laan, G. X-ray circular dichroism as a probe of orbital magnetization. *Phys. Rev. Lett.* **1992**, *68*, 1943.

(48) Nekrasov, I.; Keller, G.; Kondakov, D.; Kozhevnikov, A.; Pruschke, T.; Held, K.; Vollhardt, D.; Anisimov, V. Comparative study of correlation effects in CaVO_3 and SrVO_3 . *Phys. Rev. B* **2005**, *72*, No. 155106.

(49) Schindler, M.; Hawthorne, F.; Baur, W. Crystal chemical aspects of vanadium: polyhedral geometries, characteristic bond valences, and polymerization of (VO_n) polyhedra. *Chem. Mater.* **2000**, *12*, 1248–1259.

(50) Shannon, R. D. Revised effective ionic radii and systematic studies of interatomic distances in halides and chalcogenides. *Acta Crystallogr., Sect. A: Found. Adv.* **1976**, *32*, 751–767.

(51) Choi, S. M.; Stringer, C. J.; Shrout, T. R.; Randall, C. A. Structure and property investigation of a Bi-based perovskite solid solution: $(1-x)\text{Bi}(\text{Ni}_{1/2}\text{Ti}_{1/2})\text{O}_3-x\text{PbTiO}_3$. *J. Appl. Phys.* **2005**, *98*, No. 034108.

(52) Randall, C.; Eitel, R.; Jones, B.; Shrout, T.; Woodward, D.; Reaney, I. Investigation of a high T_c piezoelectric system: $(1-x)\text{Bi}(\text{Mg}_{1/2}\text{Ti}_{1/2})\text{O}_3-x\text{PbTiO}_3$. *J. Appl. Phys.* **2004**, *95*, 3633–3639.

(53) Chen, J.; Wang, F.; Huang, Q.; Hu, L.; Song, X.; Deng, J.; Yu, R.; Xing, X. Effectively control negative thermal expansion of single-phase ferroelectrics of $\text{PbTiO}_3-(\text{Bi},\text{La})\text{FeO}_3$ over a giant range. *Sci. Rep.* **2013**, *3*, No. 2458.

(54) Eitel, R. E.; Randall, C. A.; Shrout, T. R.; Rehrig, P. W.; Hackenberger, W.; Park, S.-E. New high temperature morphotropic phase boundary piezoelectrics based on $\text{Bi}(\text{Me})\text{O}_3\text{-PbTiO}_3$ ceramics. *Jpn. J. Appl. Phys.* **2001**, *40*, 5999–6002.

(55) Suchomel, M. R.; Davies, P. K. Enhanced tetragonality in $(x)\text{PbTiO}_3-(1-x)\text{Bi}(\text{Zn}_{1/2}\text{Ti}_{1/2})\text{O}_3$ and related solid solution systems. *Appl. Phys. Lett.* **2005**, *86*, No. 262905.

(56) Cohen, R. E. Origin of ferroelectricity in perovskite oxides. *Nature* **1992**, *358*, 136.

(57) Kuroiwa, Y.; Aoyagi, S.; Sawada, A.; Harada, J.; Nishibori, E.; Takata, M.; Sakata, M. Evidence for Pb-O covalency in tetragonal PbTiO_3 . *Phys. Rev. Lett.* **2001**, *87*, No. 217601.

(58) Goodenough, J. B.; Zhou, J. Varied roles of Pb in transition-metal PbMO_3 perovskites ($M = \text{Ti}, \text{V}, \text{Cr}, \text{Mn}, \text{Fe}, \text{Ni}, \text{Ru}$). *Sci. Technol. Adv. Mater.* **2015**, *16*, No. 036003.

(59) Vidya, R.; Ravindran, P.; Knizek, K.; Kjekshus, A.; Fjellvåg, H. Density Functional Theory Studies of Spin, Charge, and Orbital Ordering in YBaT_2O_2 ($T = \text{Mn}, \text{Fe}, \text{Co}$). *Inorg. Chem.* **2008**, *47*, 6608–6620.

(60) Vidya, R.; Ravindran, P.; Kjekshus, A.; Fjellvåg, H. Spin, charge, and orbital ordering in the ferrimagnetic insulator YBaMn_2O_2 . *Phys. Rev. B* **2002**, *65*, No. 144422.

(61) Ravindran, P.; Vidya, R.; Eriksson, O.; Fjellvåg, H. Magnetic-Instability-Induced Giant Magnetoelectric Coupling. *Adv. Mater.* **2008**, *20*, 1353–1356.

(62) Brooks, H. Ferromagnetic anisotropy and the itinerant electron model. *Phys. Rev.* **1940**, *58*, 909.

(63) Bozorth, R. Directional ferromagnetic properties of metals. *J. Appl. Phys.* **1937**, *8*, 575–588.

(64) Scherz, A.; Wende, H.; Baberschke, K. Fine structure of X-ray magnetic circular dichroism for early 3d transition metals. *Appl. Phys. A: Mater. Sci. Process.* **2004**, *78*, 843–846.

(65) Wende, H. Recent advances in X-ray absorption spectroscopy. *Rep. Prog. Phys.* **2004**, *67*, 2105.

(66) Scherz, A.; Wende, H.; Sorg, C.; Baberschke, K.; Minr, J.; Benea, D.; Ebert, H. Limitations of integral XMCD sum-rules for the early 3d elements. *Phys. Scr.* **2005**, 586.

(67) Wende, H.; Scherz, A.; Sorg, C.; Baberschke, K.; Gross, E.; Appel, H.; Burke, K.; Minár, J.; Ebert, H.; Ankudinov, A.; Rehr, J. XMCD analysis beyond standard procedures. *AIP Conf. Proc.* **2007**, *882*, 78–82.